COBEM 2023 27TH INTERNATIONAL CONGRESS OF MECHANICAL ENGENEERING
ABCM Brazilian Society of Mechanical Sciences and Engineering
27th ABCM International Congress of Mechanical Engineering
December 04-08, 2023, Florianópolis-SC, Brazil

COB-2023-0599
DEVELOPMENT OF A DEVICE FOR ILIAC VEIN CLOT REMOVAL

Amanda Souza Fernandes
Vitória Bento Botelho
Gabriel Felipe de Faria
Luiz Renato Brumati
João de Sá Brasil Lima
Instituto Mauá de Tecnologia, Praça Mauá, 01, São Caetano do Sul
amasf270400@gmail.com
vivi.bbotelho@gmail.com
g_faria@icloud.com
luizrenatobrumati23@gmail.com
joão.brasil@maua.br

Abstract. *Cardiovascular disease cases have grown by 93% since 1990, reaching 550 million people worldwide last year. Coronary artery disease and stroke are the leading conditions causing the most deaths, both related to thrombosis. This disorder obstructs the lumen of the vessels, decreasing tissue's oxygenation. Depending on the diagnosis, this condition treatment occurs mainly through pharmacological therapies or surgical procedures. The study focuses on a surgical method called thrombectomy, which may use mechanical or suction techniques on iliac vein drainage, mainly affected in people who suffer from May-Thurner syndrome. The approach adopted was the analysis through Computational Fluid Dynamics, which solves the flow field via Navier-Stokes, respecting the blood nonlinear deformation modeled by Carreau-Yasuda. The geometry was simulated under a pulsatile blood flow condition, considering a 310 K temperature and a 0.70 L/min volumetric flow rate. The pressure and velocity results were from 6 mmHg and 15 to 104 cm/s, respectively, with a shear rate ranging from 0 to 20 Nm-2. This study analyzed the flow in the vein considering clot obstruction at 70% and how the device reacts to being under the pressure field of the flow.*
Keywords: *blood clot, thrombectomy device, biofluid dynamics, Computational Fluid Dynamics.*

1. INTRODUCTION

Cardiovascular Disease (CVD) cases are increasing year by year. In 2022, a British organization estimated that 1 in 14 people suffer from cardiovascular conditions, resulting 550 million individuals worldwide. That means the number has statistically increased by 93% since 1990, when only 285 million people were affected. This trend is due to the growth and aging of the world's population, aside from the current lifestyle. However, survival rates have improved for some diseases, such as heart attacks and strokes, despite the higher prevalence of patients (British Heart Foundation, 2022).

Figure 1. Heart and Circulatory Disease Worldwide, British Heart Foundation (2022).

Diseases classified as cardiovascular are cataloged in Chapter IX of the International Statistical Classification of Diseases and Related Health Problems (CID-10), prepared by the World Health Organization (WHO). Some of the described conditions in the document affect the hemostasis balance, resulting in abnormal clot formation known as thrombosis. Due to veins and artery obstruction, this pro-thrombotic state may cause serious diseases, such as heart attack, stroke, and pulmonary embolism (Douketis, 2022). The thrombi formation can originate from hereditary or acquired

health problems. The medical bibliography identifies three main mechanisms: thrombophilia, endothelial damage, and abnormal blood flow, Virchow's Triad (Kumar, Abbas e Aster, 2016).

Thrombophilia is characterized by genetic disorders or external factors imposed on the subject that result in a hypercoagulable blood condition (Correa et al., 2019). As for tissue damage, in opposition to the natural coagulation cascade activation, to prevent bleeding, the cells that define the coagulation stage may be modified to a pro-thrombotic state, called endothelial activation, without suffering any trauma. Finally, irregular blood flow is caused by some diseases, such as coronary artery disease and iliac vein compression syndrome (ILVC), such as generating recirculation zones and coagulation due to stasis (Kumar et al., 2016).

The methods used in thrombosis treatment consist of prescribing antithrombotic drugs and thrombolytic agents to prevent the development and stimulate clot dissolution, respectively (Watson et al., 2016). Another option for vessel clearance is catheter-guided surgical intervention, known as thrombectomy, a procedure with three main removal techniques: suction, self-expanding stent, and a combination of both (Conitec, 2021). Even though all methods have risks, including bleeding and thrombosis recurrence in the pharmacological treatment in addition to trauma and vessel wall collapse in the case of a thrombectomy, the treatment choice depends on a careful evaluation of the patient by a health professional (Brandão, et al., 2013; Ismail, et al., 2022; Munich, et al., 2019).

Therefore, studies to improve patients' safety and life quality are becoming more common. Among the medical contributions is the computational simulation of biological flows. This tool allows researchers to understand the blood behavior in the circulatory system and to evaluate essential parameters, such as velocity gradient, pressure, and shear stress, assisting in hospital device development and optimization (Doost, et al., 2016; Versteeg and Malalasekera, 2007). Blood is a non-Newtonian fluid that shows variation in viscosity according to temperature, this occurs because it is composed of two phases: plasma and formed elements (Carvalho, 2022).

The chosen study location is the left common iliac vein, where ILVC (or May-Thurner syndrome) facilitates thrombus formation, a phenomenon observed in 18-49% of the patients with deep vein thrombosis (Andrade, et al., 2017). Thus, blood flow was evaluated through Computational Fluid Dynamics (CFD), particularly ANSYS Fluent, to verify the clot effects and propose improvements in the thrombectomy devices. With this purpose, the Navier-Stokes equations were used to solve the movement quantity conservation and the Carreau-Yasuda model to capture the change in viscosity.

2. METHODOLOGY

According to Carvalho (2022), a Newtonian fluid is characterized by its viscosity as a function of temperature, regardless of the shear velocity applied, while a non-Newtonian fluid has a variation in viscosity with an increase in shear velocity. In the context of hemodynamic simulations performed in this study, blood will be considered a Newtonian fluid in the analysis of the permanent regime (steady state) and a non-Newtonian fluid in the transient flow regime (pulsatile) and the fluid-structure interaction simulation.

The researchers calculated Reynolds to determine whether the two regimes' flow was laminar or turbulent, according to Eq. 1. The results are in Table X, showing that both flows are laminar, as the result remained below the transition limit of 2300 for internal flows (White, 2018).

$$Re = \frac{DV\rho}{\mu} = \frac{\text{Average velocity} \times \text{Diameter}}{\text{Kinematic viscosity}} \tag{1}$$

For the permanent and transient flow regimes, the Navier-Stokes equation (Eq. 2) is the basis for addressing problems related to their behavior.

$$\rho \frac{DV}{Dt} = -\nabla p + \rho \vec{g} + \mu \nabla^2 \vec{V} \tag{2}$$

As for the permanent regime flow analysis, considering that the fluid occurs laminarly in cylinders of a constant section, the Poiseuille equation gives the analytical solution for the pressure difference. Thus, it is also possible to describe the velocity profile for this flow by simplifying the Navier-Stokes equations, where for the case of this study, whose flow is stationary, acceleration effects are neglected, the fluid properties are constant, and the vessel wall is an elliptical form, uniform, and stationary. The velocity profile is described by Eq. 3 (Boussinesq, 1868).

$$u(y,z) = \frac{G}{2\mu\left(\frac{1}{a^2}+\frac{1}{b^2}\right)}\left(1-\frac{y^2}{a^2}-\frac{z^2}{b^2}\right) \tag{3}$$

The transient analysis was considered the Carreau-Yasuda model, the most common model for pseudoclassical fluids in hemodynamic simulations, since it works for lower and higher values of strain rates (BOYD, BUICK, and GREEN, 2007). That model can be described by Eq. 4.

$$\eta(\dot{\gamma}) = \eta_\infty + (\eta_0 - \eta_\infty)(1 + (\lambda\dot{\gamma})^a)^{\frac{n-1}{a}} \tag{4}$$

2.1 Vein geometry and ANSYS Meshing

The geometry analyzed was adapted from the model presented in the research by Rahbar, et al. (2010), represented in grey, where the blood vessel segment is composed of the Infrarenal Vena Cava (IVC), Left Iliac Vein (LIV), Right Iliac Vein (RIV) and the renal veins. The renal veins and the suprarenal section of the vena cava have been removed from the reference geometry (Fig. 1) since this study focuses on the iliac vein region. In addition, the curvature in the studied vein, caused by the curvature of the spine, was removed, simplifying the model.

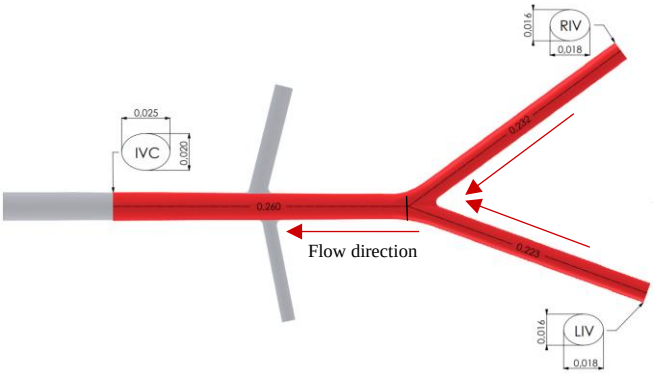

Figure 1. Iliac vein geometry in meters.

Using ANSYS Meshing, the fluid domain was discretized. By verifying the convergence of the mesh, the goal was to obtain an optimal relationship between the performance and computational cost of the model. Therefore, was estimated the error due to discretization using the Grid Convergence Method based on Richardson's extrapolation method, which has as a product an error indicator index called GCI (Celik, 2008). The methodology, described in detail by Celik et al. (2008) and Bordin (2014), consists of five main steps where a set of three meshes with different degrees of refinement are generated and then simulated under the boundary conditions of the problem, evaluating the behavior of the parameters of interest. Thus, the initial step was generating a coarse mesh and then determining its representative size h, where three-dimensional analysis can be determined using Eq. 3.

$$h_{(1,2,3)} = \left[\frac{1}{N}\sum_{i=1}^{N}(\Delta V_i)\right]^{\frac{1}{3}} \tag{5}$$

where N is the number of total cells, and V_i is the unit volume of the ith cell.

Next, the refinement factor r was determined based on the ratio between the parameters h of the evaluated mesh pair, according to the following relations: $r_{21} = h_2/h_1$; $r_{32} = h_3/h_2$. Empirically, to obtain satisfactory results, the r factor must have a value equal to or greater than 1.3 (Celik, 2008). Thus, adopting the minimum necessary r factor and based on the information of the number of cells of the coarse mesh, it is possible to estimate the size of the intermediate and fine meshes, considering that the variation of the volume between the meshes is minimal, the initial volume is kept constant, and corrected at the end of the process. Table 1 presents the final three configurations' parameters of the mesh.

Table 1. Mesh convergence test parameters.

Mesh refinement	Number of elements	Geometry volume [mm^3]	r_{21}, r_{32}
Coarse	2977683	19.236	
Medium	1180920	19.258	1.36, 1.35
Fine	479622	19.269	

The apparent order p for the method was also determined from Eq. 5 and , where Φ_k is the value of the variable of interest resulting from the simulation for the kth mesh, and s is a variable, whose value results from a test of the sign of the ratio $\Delta\Phi_{32}/\Delta\Phi_{21}$, resulting in a value equal to -1 for a negative sign, 0 for a null ratio and 1 if it is positive.

$$p = \frac{1}{\ln(r_{21})}\left|\ln\left|\frac{\Phi_3 - \Phi_2}{\Phi_2 - \Phi_1}\right|\right| + q(p), \tag{6}$$

$$q(p) = \ln\left(\frac{r_{21}^p - s}{r_{32}^p - s}\right), \tag{7}$$

Finally, according to Eq. 7 was determined the GCI index value for both mesh pairs. For the following parameters was assessed the mesh convergence: pressure variation between outlet and mean inlet pressure ΔP; maximum velocity in the measurement lines in each venous segment U_{MAX}.

$$GCI_{21} = \frac{1.25|\Delta\Phi_{21}/\Phi_1|}{r^p - 1};\ GCI_{32} = \frac{1.25|\Delta\Phi_{32}/\Phi_2|}{r^p - 1}, \tag{8}$$

The intermediate mesh was selected considering the results presented in Table 2 since the percentage error related to mesh refinement GCI_{32} is small for all variables, and the gain in accuracy concerning the most refined mesh GCI_{21} is insignificant, as it would be required extra computational effort.

Table 2. GCI results for the variables of interest.

Index	ΔP	U_{MAX} IVC	U_{MAX} RIV	U_{MAX} LIV
GCI_{21} [%]	0,013	0,013	0,029	0,142
GCI_{32} [%]	0,018	0,017	0,014	0,169

Once the ideal mesh size for the analysis was determined, its quality was also verified from the Skewness metric that provides a perspective of the distortion of the internal angles of the element, where values closer to 0 on the scale indicate elements closer to the ideal (equilateral or equiangular). The analyzed mesh presents a maximum value of 0.63 on the Skewness scale, which falls within an acceptable quality window for CFD analyses according to Ansys, 2022. Figure 2 shows the discretized fluid volume with the mesh details and the indications of the gauging sections of the velocity profiles A, B, and C.

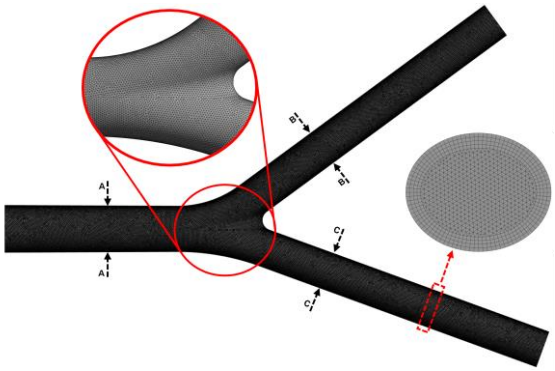

Figure 2. Mesh details.

2.2 Clot and device geometry

The device's geometry (Fig. 3) was developed based on the reference to the commercial "MERCI" device. It consists of a long thin wire with a helical coil formed at the distal end. The idea of the proposed device is to follow the spiral model but with nine wires to have more excellent protection when removing the clot if any fragments come off. In this case, the wires would play the role of a protective net, preventing this clot fragment from falling into the bloodstream and potentially causing a pulmonary embolism.

The Nitinol is the material chosen for the device. This material is Nickel-Titanium (Ni-TI) and is commonly used for clinical, dental, and medical use, mainly due to its biocompatibility. It also has elastic recovery, low rigidity,

superelasticity, thermoactivation and, most notably for the choice of this material, the shape memory effect (SMA) (Sertório, 2018).

This shape memory effect (Fig. 4) ensures that the device can pass through the body's veins fully stretched inside the catheter, and only when it exceeds the blood clot is released from inside the catheter. When it encounters the blood, due to its higher temperature, it returns to the shape it was originally produced in, in this case, the spiral shape.

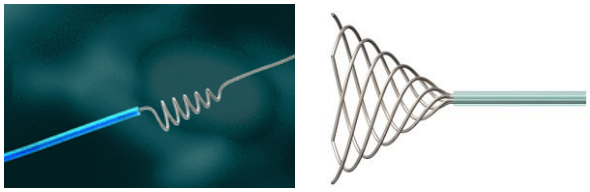

Figure 3. Proposed device.

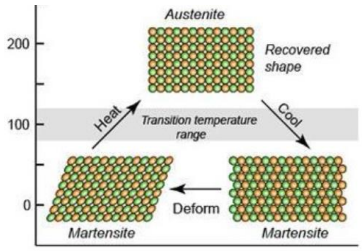

Figure 4. Representation of Nitinol's memory shape (Ansys, 2023).

The clot was modeled by the authors considering an obstruction of 70% in the iliac vein (Fig. 5).

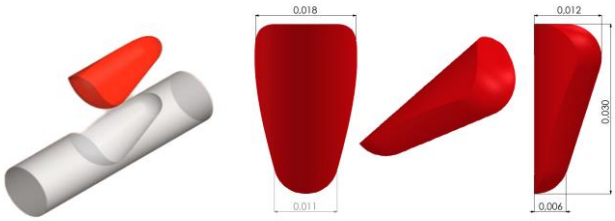

Figure 5. Modeled blood clot obstructing the vein by 70%, measurements in meters.

Figure 6 shows a model of how the proposed device would remove the clot. Once the device is released, it will pull the clot in the opposite direction to the blood flow.

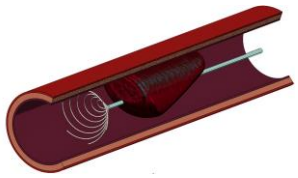

Figure 6. Model of the proposed device removing the clot inside the iliac vein.

In the case of the clot and device mesh, the converged GCI base mesh was used for the fluid part. Still, the mesh in the device region was refined for CFD, as was the device itself in Finite Element Analysis, which the FSI analysis utilizes.

2.3 ANSYS Fluent

The first simulation consisted of analyzing, in a permanent regime, a vein in average conditions. In other words, it was considered healthy. Then, the simulation in a pulsatile regime considered the vein with the blood clot and the proposed device. Table 3 shows the parameters used as inputs for both simulations.

Table 3. General parameters.

Input Parameters	**Author's Values**	**Values by Rahbar, et al. (2010)**
Axial length of the vessel of the RIV (L_R)	0,232 m	Rahbar, et al. (2010)
Axial length of the vessel of the LIV (L_L)	0,223 m	Rahbar, et al. (2010)
Major axis of the elliptical geometry – inlet (a_i)	0,018 m	Rahbar, et al. (2010)
Minor axis of the elliptical geometry - inlet (b_i)	0,016 m	Rahbar, et al. (2010)
Major axis of the elliptical geometry – outlet (a_o)	0,025 m	Rahbar, et al. (2010)
Minor axis of the elliptical geometry – outlet (b_o)	0,020 m	Rahbar, et al. (2010)
Reynolds numbers – inlet (Re_i)	313	Authors
Reynolds numbers - outlet (Re_o)	211	Authors

In the permanent regime analyses, the fluid assumed Newtonian behavior, characterized by constant viscosity, which, as well as the specific mass, were adopted according to the values presented by Rahbar (2010). The condition of sliding on the walls of the blood vessel was disregarded, implying that the fluid adheres to the walls and assumes its velocity, which is zero due to the adoption of the blood vessel structure as rigid.

The input conditions were defined based on an average mass flow value for each iliac vein, also based on the study by Rahbar (2010). The outflow condition was established for the outlet since the flow velocity and pressure are unknown a priori in this region. So, the solver determines these conditions without additional parameters defined (ANSYS, 2013). Finally, Table 4 describes the values adopted for each parameter.

Table 4. Permanent Flow Regime parameters.

Parameters	**Values**	**Reference**
Average velocity – inlet (V_{pi})	0,0501 m/s	Authors
Average velocity - outlet (V_{po})	0,0577 m/s	Authors
Dynamic viscosity (μ_p)	0,004 kg/m.s	Rahbar, et al. (2010)
Density (ρ_p)	1000 kg/m³	Rahbar, et al. (2010)
Inlet boundary conditions ($\dot{m}_p$)	0,01133 kg/s	Rahbar, et al. (2010)
Outlet boundary conditions	Outflow	Authors

For the transient regime, the blood flow inside the vein was considered laminar, with its non-Newtonian characteristics described by the Carreau-Yasuda model. In addition, the flow profiles (Inlet) and pressure profiles (Outlet) were also used as boundary conditions to represent the cardiac cycle at the study site.

The Inlet used an infrarenal pulsatile flow like that measured in the study by Corbellini (2012), which was divided equally between the iliac veins (Figure 18). The curve represents the flow of blood in the iliac vein over a cardiac cycle with a period of 0.8 seconds in a person at 72 bpm (beats per minute), according to Bhowmick, Hasan, and Hasan (2019).

For the data to incorporate into ANSYS Fluent, the flow values were calculated in L/min in Excel, with 0.02 seconds of interval, and converted to mass flow using a density of 1000 kg/m3 as a reference.

Equation 9 represents the 6th-degree polynomial that describes the pulsatile flow through the trend line.

$$\dot{m} = 2{,}26x^6 - 12{,}38x^5 + 19{,}86x^4 - 13{,}51x^3 + 3{,}97x^2 - 0{,}37x + 0{,}01 \quad (9)$$

For Output, we considered the pressure profile in the right atrium, where the vena cava flows, which tends to vary between 0 and 5 mmHg in an alternating phase concerning blood flow. To adopt this hypothesis, the geometry of the inferior vena cava extends from the iliac vein to the right atrium, being the lengths based on the study by Takayama, Hirai, et al. (1993).

Through a system of 1st-degree equations the pressure profile over time was obtained, which correlates pressure with the flow, as indicated in Equation 10, resulting in P=-8782,456m ˙+886,506.

$$\begin{cases} 853{,}261 = a \cdot 0{,}004 + b \\ 333{,}305 = a \cdot 0{,}063 + b \end{cases} \quad (10)$$

Finally, Equation 9 was substituted into the resulting pressure expression to observe the pressure variation over time (Figure 18), as shown in Equation 11.

$$P = -39681t^6 + 217383t^5 - 348769t^4 + 237363t^3 - 69767t^2 + 6567{,}5t + 886{,}5 \quad (11)$$

Finally, Table 5 summarizes the boundary conditions adopted for the simulation in the transient regime.

Table 5. Transient Flow Regime parameters.

Parameters	Values	Reference
Inlet boundary conditions	Flow profiles	Authors
Outlet boundary conditions	Pressure profiles	Authors

3. RESULTS

3.1 Permanent flow regime

The flow result was regular, with no evidence of apparent backflow, even in the region where the iliac veins meet the inferior vena cava. In addition, the pressure gradient shown in Figure X favors the flow, as expected, and results in a maximum pressure difference of 6.96 Pa for the stretch studied.

Concerning the velocity field, the flow accelerates along the extended stretches in the iliac vein entrance regions until it reaches full development. This is characterized by the convergence of the simulation velocity profile to the theoretical profile described by Poiseuille, as illustrated in Figure 7.

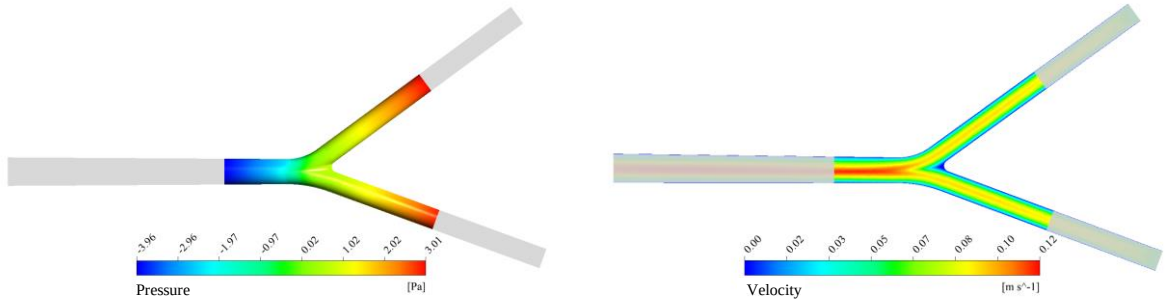

Figure 7. Pressure gradient and velocity field in the region studied.

Subsequently, the flow begins to develop again as it approaches the confluence region in the inferior vena cava since the ratio between the increase in flow and the reduction in total area is positive, thus satisfying the continuity relationship and reaching a maximum speed of 0.12 m/s, shown in Figure x.

Figure 8 plots the curves comparing the velocity profiles of the elliptical section of the iliac veins (LIV and RIV) and the vena cava compared to the theoretical profiles. It is possible to notice a variation between the numerical and theoretical results; this deviation may be due to the incomplete flow development along the veins. The maximum errors are 5.61% and 6.69% for the LIV and RIV sections, respectively, and 1.36% for the IVC. All results were below the acceptable value of 10% adopted by the authors.

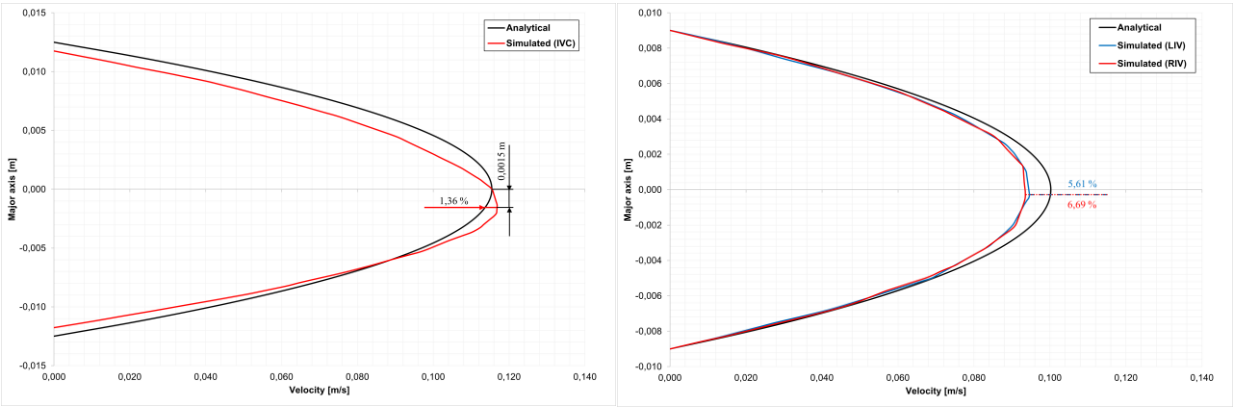

Figure 8. Comparison between theoretical and simulated velocity profiles for vena cava (left) and iliac veins (right).

Analogous to Figure 8, Figure 9 presents the curves comparing the simulation with the analytical solution of the velocity at the centerline of the iliac veins (LIV and RIV) and the vena cava. The maximum errors were 49,93%, 49,76%, and 30,80% for the LIV, RIV, and IVC respectively.

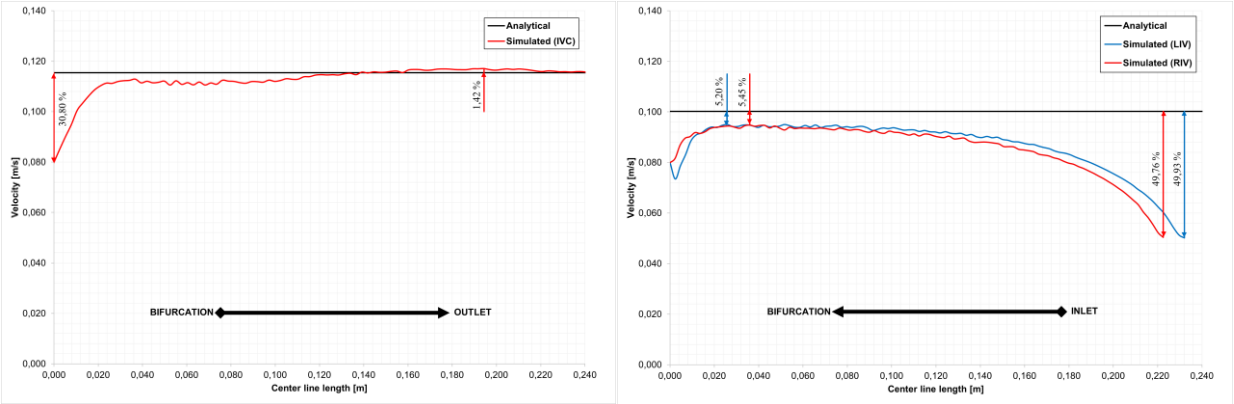

Figure 9. Comparison between the simulated velocity in the center line along the iliac veins with the centerline velocity for the theoretical Poiseuille flow.

.

The Strain Rate (SR) and Wall Shear Stress (WSS) distributions (Fig. 10) behaved as expected, with the highest values found in the regions of higher disturbance in the flow, being in the region of the confluence of the iliac veins in the vena cava, in addition to the inlet regions. However, since this behavior is due to the region of development of the flow, they are dismissed.

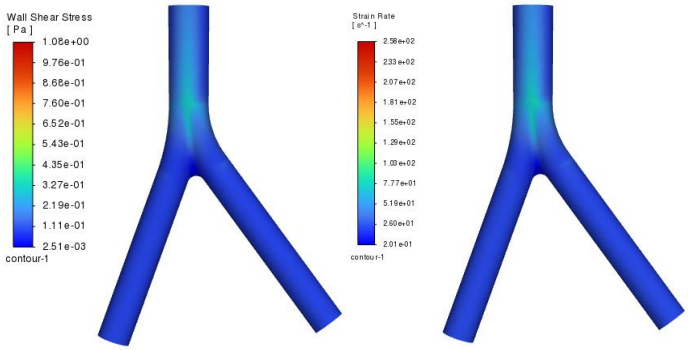

Figure 10. WSS and SR distribution on vein's walls

Table 6. Simulation results for the permanent flow regime.

Parameters	**Values**
Maximum pressure	3.01 Pa
Maximum Speed	0.12 m/s
Maximum wall shear stress	1.08 Pa
Maximum strain rate	2.58e2 s^-1

3.2 Transient flow regime

In the case of the transient simulation, Figure 11 shows the results. The pressure gradient shown in Figure 11 favors flow, as expected, and results in a maximum pressure difference of 858.39 Pa for the stretch studied, more than 200% higher than the result for the healthy vein.

Concerning the velocity field, the value was also higher than the permanent analysis, resulting in 0.20 m/s, where there is a decrease in the vein area just after the clot.

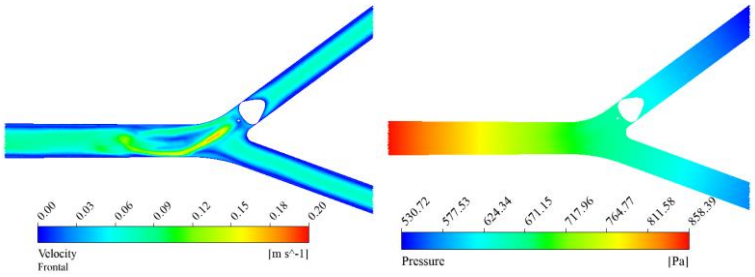

Figure 11. WSS and SR distribution on vein's walls

Table 7 shows the FSI result values.

Table 7. Simulation results for the transient FLOW regime.

Parameters	Values
Maximum pressure	858.39 Pa
Maximum Speed	0.20 m/s

3.3 FSI (Fluid-Structure Interaction)

The pressure load calculated in CFD was imported into ANSYS Mechanical® to check the mechanical behavior of the devices when immersed in blood flow. With this one-way coupling, it is possible to check the stresses and strains acting on the object of study, evaluating the effects of the flow on the clot remover.

The tensile strength of Nitinol varies from 195 to 690 Mpa (Ansys, 23). It is, therefore, possible to observe that the device is within the expected range since its maximum stress was approximately 0.31 Mpa. As for the maximum deformation, it did not obtain a significant value, reaching approximately 0.00072 mm. Figure 12 presents those results.

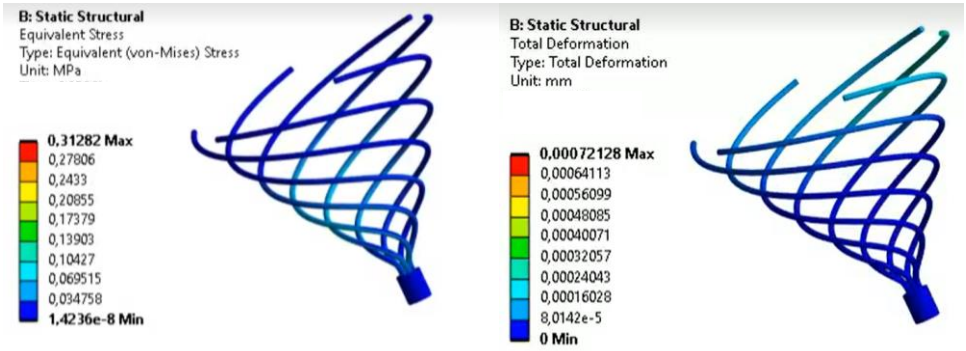

Figure 12. WSS and SR distribution on vein's walls

Table 8 shows all the FSI result values.

Table 8. Simulation results for the FSI.

Parameters	Author's Values
Highest stress equivalent value	0,31 m
Highest deformation value	m

4. CONCLUSION

This study analyzed the flow in the iliac vein together with the inferior vena cava in permanent and transient regimes to develop a device for removing clots in this area. With the results of these analyses, it was possible to validate a new stent geometry for clot removal through an FSI analysis. This last analysis showed that the maximum stress in the device when facing the flow of a vein with a clot, does not exceed its flow limit. The same applies to its maximum deformation,

which is of a non-significant order. With these evaluations, it was possible to test the initial viability of the concept of this new device.

5. REFERENCES

Ansys, 2023. GRANTA EduPack software, ANSYS, Inc., Cambridge, UK, YEAR (www.ansys.com/materials). Accessed: September 20, 2023

Ansys, 2022. *Ansys meshing user's guide*, https://ansyshelp.ansys.com. Accessed: June 03, 2023.

Andrade, Y. C., Sarubi, T. R. B., Cuollo, M. C., Okunahara, A., 2017. Endovascular treatment of deep venous thrombosis related to May-Thurner syndrome (in Portuguese). *Medical Journal of Minas Gerais, Belo Horizonte*, Vol. 27, p. 75 – 79. Deposit: January 31, 2017.

Boussinesq, J., 1868. Mémoire sur I"influence des frottements dans les mouvements réguliers des fluids, *Journal de mathématiques pires et al appliquées*, Vol. 13, p. 377-424.

Bordin, F. S., 2014. Analysis of the effect of fluid-structure interaction on fluid dynamic forces in a 3D flexible blade element. M.Sc thesis, Graduate *Program in Mechanical Engineering, Federal University of Rio Grande do Sul, Porto Alegre, Brasil*.

Boyd, Joshua, Buick, James M., Green, Simon. 2007. *Analysis of Casson and Carreau-Yasuda Non-Newtonian Blood Models in Steady and Oscillatory Flows Using The Lattice Boltzmann Method*. 2007.

Brandão, G.M.S., Cândido, R. C.F., Rollo, Hamilton A., Sobreira, M. L., Junqueira, D. R., 2018. "Direct oral anticoagulants for the treatment of deep vein thrombosis: review of systematic reviews (in Portuguese)". *Jornal Vascular Brasileiro*. Deposit: October 10, 2018.

Bhowmick, Dhiman, Hasan, Md Toukir e Hasan, A B M Toufique. 2019. Non-Newtonian pulsatile blood flow dynamics around a Y-junction. *AIP Conference Proceedings*.

Celik, I. B., Ghia, U., Roache, P. J., Freitas, C. J., Coleman, H., Raad, P. E., 2008. *Procedure for Estimation and Reporting of Uncertainty Due to Discretization in CFD Applications*. Deposit: July 22, 2008.

Corbellini, Peixer, M. 2012. *Estudo experimental do desempenho de um novo filtro de veia cava inferior. Universidade Federal de Santa Catarina*. Florianópolis: s.n., 2012. p. 111.

Correa, L. S., Tiecher, P.B., Silva, I. R. V. D., 2019. Hereditary and acquired thrombophilia in pregnant women (in Portuguese). *6th International Congress on Health*.

Doost, S. N., Ghista, D., Su, B., Zhong, L., Morsi, Y.S., 2016. *Heart Blood Flow Simulation: A Perspective Review. Biomedical Engineering*, Singapura, p. 1 – 28.

Douketis, J., 2022, *Deep Vein Thrombosis (in Portuguese), Manual MSD*, https://www.msdmanuals.com/pt-br/casa/dist%C3%BArbios-do-cora%C3%A7%C3%A3o-e-dos-vasos-sangu%C3%ADneos/dist%C3%BArbios-venosos/trombose-venosa-profunda-tvp. Acessed: 05 Jun 2023.

Ismail, U., Rowe, R. A., Cashin, J., Genin, G. M., Zayed, M. A., 2022. *Multimodal thrombectomy device for treatment of acute deep venous thrombosis*. Scientific Reports, São Luís, United States. Deposit: March 28, 2022.

Kumar, V., Abbas, Abul K., Aster, Jon C., 2016. *Pathology – Pathological bases of diseases (in Portuguese).*

Munich, S. A., Vakharia, K., Levy, E. I., 2019. Overview of Mechanical Thrombectomy Techniques. *Neurosurgery*, New York p. 560-567. Deposit: July 01, 2019.

Rahbar, E., Mori, D., Moore, J. E., 2010. Three-dimensional Analysis of Flow Disturbances. *Society of Interventional Radiology, Fairfax*. Deposit: December 24, 2010.

Takayama, Toshimasa, et al. 1993. Measurement of the Vena Cava at Postmortem Examination, From the Upper End of the Superior Vena Cava Via the Right Atrium to the Lower End of the Inferior Vena Cava, *Clinical Anatomy: The Official Journal of the American Association of Clinical Anatomists and the British Association of Clinical Anatomists*, Vol. 6, pp. 349-352.

Sertório, A. R., 2018. *Ligas Ni-Ti (Nitinol) com Efeito Memória de Forma – Futuro ou Utopia?*. Trabalho de Formatura - Escola Politécnica da Universidade de São Paulo. Departamento de Engenharia Metalúrgica e de Materiais. São Paulo, 2008.

Versteeg, H. K., Malalasekera, W., 2007. *An Introduction to Computational Fluid Dynamics: The Finite Volume Method*. 2ª. ed. Londres: Pearson Education Limited.

Watson, L., Broderick, C., Armon, M. P., 2016. Thrombolysis for acute ischemic stroke. *Cochrane Database of Systematic Reviews*, Leven p. 1 -71.

White, F. M., 2018, *Fluid Dynamics*, 8ªed. Mc Graw Hill Education. New York.

6. RESPONSIBILITY NOTICE

The authors are the only responsible for the printed material included in this paper.